Comparative study of the magnetic properties of $La_3Ni_2B'O_9$ for B' = Nb, Ta or Sb

Chun-Mann Chin[1], Peter D. Battle[1,*], Stephen J. Blundell[2], Emily Hunter[1], Franz Lang[2], Mylène Hendrickx[3], Robert Paria Sena[3] and Joke Hadermann[3].

1. Inorganic Chemistry Laboratory, University of Oxford, South Parks Road, Oxford, OX1 3QR, U. K.
2. Clarendon Laboratory, Dept. of Physics, University of Oxford, Parks Road, Oxford OX1 3PU
3. EMAT, University of Antwerp, Groenenborgerlaan 171, 2020 Antwerp, Belgium

* Corresponding author.

Email address: peter.battle@chem.ox.ac.uk (P. D. Battle)

Abstract

Polycrystalline samples of $La_3Ni_2NbO_9$ and $La_3Ni_2TaO_9$ have been characterised by X-ray and neutron diffraction, electron microscopy, magnetometry and muon spin relaxation (μSR); the latter technique was also applied to $La_3Ni_2SbO_9$. On the length scale of a neutron diffraction experiment, the six-coordinate sites of the monoclinic perovskite structure are occupied in a 1:1 ordered manner by Ni and a random ⅓Ni/⅔*B'* mixture. Electron microscopy demonstrated that this 1:1 ordering is maintained over microscopic distances, although diffuse scattering indicative of short-range ordering on the mixed site was observed. No magnetic Bragg scattering was observed in neutron diffraction patterns collected from $La_3Ni_2B'O_9$ (*B'* = Nb or Ta) at 5 K although in each case μSR identified the presence of static spins below 30 K. Magnetometry showed that $La_3Ni_2NbO_9$ behaves as a spin glass below 29 K but significant short-range interactions are present in $La_3Ni_2TaO_9$ below 85 K. The contrasting properties of these compounds are discussed in terms of their microstructure.

Introduction

Several mixed-metal oxides adopt a monoclinic form of the well-known perovskite structure [1]. In many such cases, the six-coordinate sites are occupied by two different cations, *B* and *B'*. When *B* and *B'* differ significantly in size or charge they will have different coordination requirements and they are therefore expected to adopt an ordered arrangement over multiple crystallographic sites. The monoclinic space group most commonly adopted, $P2_1/n$, has two suitable sites with equal multiplicities and cation ordering is therefore readily achieved for compounds with the general formula $A_2BB'O_6$. However, a number of compounds with the general formula $A_3B_2B'O_9$ also adopt this space group, despite the apparent incompatibility between the 1:1 ratio of sites and the 2:1 ratio of six-coordinate cations. In many of these cases, for example $La_3Ni_2SbO_9$ [2] and $La_3Ni_2NbO_9$ [3], a partial ordering occurs in which one site is occupied only by *B* and the other site by 33 % *B* and 67 % *B'*. The nearest-neighbour (NN) magnetic superexchange in these compositions is not frustrated by the magnetic dilution of the *B'* site and the *B* – O – *B* interaction is expected to be antiferromagnetic. However, because there are unequal numbers of magnetic cations on the two sites, a ferrimagnet is expected to result. We have shown that this prediction is fulfilled in the case of $LaSr_2Cr_2SbO_9$ [4].

Unfortunately, not all the comparable compositions studied to date behave in the same way. $SrLa_2Ni_2TeO_9$ [5] has been described as a spin glass with small regions of magnetic order present in the crystallites and $CaLa_2Ni_2WO_6$ [6] as a spin glass with no long-range magnetic order. $La_3Ni_2SbO_9$ has been studied in somewhat more depth [2, 7]. Magnetometry suggested that the compound has a spontaneous magnetisation, *i.e.* it is a ferromagnet or ferrimagnet, below ~100 K but our initial neutron diffraction experiments failed to identify any magnetic Bragg scattering. However, magnetic scattering was observed when the measurements were repeated in an external magnetic field. Furthermore, high-resolution transmission electron microscopy revealed variations in the Ni/Sb distribution in the crystallites. In order to account for these observations we developed a model in which the antimony-rich regions serve as domain walls between ferrimagnetic microdomains which are randomly aligned unless an external field is applied. By analogy with relaxor ferroelectrics we described $La_3Ni_2SbO_9$ as a relaxor ferromagnet. Below we report the results of our investigation of the magnetic properties of $La_3Ni_2NbO_9$ and $La_3Ni_2TaO_9$ by X-ray and neutron diffraction, electron microscopy, magnetometry and muon spin relaxation. The latter technique has also been applied to $La_3Ni_2SbO_9$ to enable a comparison to be made. The principal chemical difference between these compositions and $La_3Ni_2SbO_9$ is that the diamagnetic cation on the six-coordinate sites, Nb^{5+} or Ta^{5+}, has a d^0 electron configuration whereas Sb^{5+} is a d^{10} cation; there is evidence [8, 9] to suggest that this change can have a significant effect on the properties of a compound. However, we shall show below that the contrast between $La_3Ni_2NbO_9$ and $La_3Ni_2TaO_9$ is greater than that between $La_3Ni_2TaO_9$ and $La_3Ni_2SbO_9$.

Experimental

$La_3Ni_2NbO_9$ and $La_3Ni_2TaO_9$ were prepared by mixing and grinding stoichiometric amounts of pre-dried La_2O_3, NiO and Nb_2O_5 or Ta_2O_5 in an agate mortar and pestle. The mixture was then pelletised and heated in air. The niobium-containing mixture was initially heated at 1200 °C for 7 days and finally at 1250 °C for 8 days whilst that containing tantalum was heated at 800 °C for 24 hours then at 1250 °C for 11 days. The pellets were ground and reformed every 48-72 hours.

X-ray and neutron powder diffraction (XRPD and NPD) patterns were collected from both reaction products. XPRD data were collected with Cu $K_{\alpha 1}$ radiation (λ = 1.54051 Å) using a PANalytical Empyrean diffractometer operating at room temperature. NPD data were collected at selected temperatures using the diffractometer D2b (λ ~ 1.59 Å) at ILL, Grenoble; unit cell parameters determined by X-ray diffraction were used to determine

accurately the neutron wavelength. The angular ranges covered were $15 \leq 2\theta/° \leq 125$ and $10 \leq 2\theta/° \leq 150$ respectively, with step-sizes, $\Delta 2\theta$, of 0.0066 ° and 0.05 °. The Rietveld method [10], as implemented in the GSAS [11] program suite, was used to analyse the diffraction patterns. In all refinements, the background and peak shapes were modelled by a 12-term shifted Chebyshev function and a pseudo-Voigt function, respectively. Further high-intensity NPD patterns were collected using the diffractometer D1b ($\lambda \sim 2.52$ Å) at ILL.

Both compounds were also studied by transmission electron microscopy (TEM) and scanning electron microscopy (SEM). Specimens for TEM were prepared by crushing the powder in ethanol and depositing a few drops of this solution on a copper grid covered with a holey carbon film. Selected area electron diffraction (SAED) patterns were taken with Philips CM20 and FEI Tecnai G2 instruments. High angle annular dark field stem (HAADF-STEM) images and energy dispersive X-ray (EDX) maps were acquired with an FEI Titan 80-300 "cubed" microscope equipped with a Super-X detector and operated at 300 kV. Specimens for SEM were prepared by smearing the powder over tape which was mounted on a stub of metal. SEM images were collected using a JEOL 5590 microscope.

The magnetic properties of both $La_3Ni_2NbO_9$ and $La_3Ni_2TaO_9$ were determined using a SQUID magnetometer. The magnetic susceptibility was measured in fields of 10, 100 and 1000 Oe over the temperature range $2 \leq T/K \leq 300$ after cooling the sample in zero field (ZFC) and after cooling in the measuring field (FC). The variation of the magnetisation per formula unit (f.u.) with applied magnetic field was measured at 5, 150 and 220 K over the range $-50 \leq H/kOe \leq 50$. The ac susceptibility was measured in an oscillating field of amplitude 3.5 Oe over the temperature range $2 \leq T/K \leq 150$ at frequencies of 1, 10 and 100 Hz.

Zero-field muon-spin relaxation (ZF μSR) measurements were made on polycrystalline samples of $La_3Ni_2B'O_9$ (B'= Sb, Nb, Ta) using the general purpose surface (GPS) spectrometer at the Swiss Muon Source and the EMU instrument at the STFC ISIS facility. For the measurement, the samples were mounted in silver foil packets and placed on silver backing plates. In a μSR experiment, spin-polarized positive muons are stopped in a target sample, where the muon usually occupies an interstitial position in the crystal. The observed property in the experiment is the time evolution of the muon spin polarization, the behavior of which depends on the local magnetic field at the muon site, as the muon spin Larmor precesses around this field. Each muon decays, with an average lifetime of 2.2 μs, into two neutrinos and a positron, the latter particle being emitted preferentially along the instantaneous direction of the muon spin at decay. Recording the time dependence of the

positron emission directions therefore allows the determination of the spin-polarization of the ensemble of muons. Detectors placed forward (F) and backward (B) of the initial muon polarization direction record the number of positrons as a function of time following the muon implantation. The results are stored in histograms $N_F(t)$ and $N_B(t)$. The quantity of interest is the decay positron asymmetry function, defined as $A(t)=(N_F(t)-\alpha_{exp}N_B(t))/(N_F(t)+\alpha_{exp}N_B(t))$, where α_{exp} is an experimental calibration constant. $A(t)$ is proportional to the spin polarization of the muon ensemble.

Results

Preliminary analysis of the XRPD data of both reaction products suggested that each was dominated by the desired perovskite-like phase, the reflections from which could be accounted for in the monoclinic space group $P2_1/n$ with $a \sim b \sim \sqrt{2}a_p$, $c \sim 2a_p$ and $\beta \sim 90$ ° where a_p is the cell parameter of a primitive cubic perovskite. The crystal structures thus contain two crystallographically distinct octahedral sites, 2*c* and 2*d*, which are occupied by Ni^{2+} and the diamagnetic, pentavalent cations. The La^{3+} cations are accommodated on a single 4*e* site and three distinct 4*e* sites are occupied by oxide ions.

In order to refine the room-temperature crystal structure of each of the two compounds, XRPD data and NPD data from D2b were analysed simultaneously. In addition to the usual atomic parameters, the distribution of Ni^{2+} and Nb^{5+} or Ta^{5+} over the six-coordinate sites was allowed to vary. The cation distribution determined in these refinements was held constant during refinements of the crystal structure based on D2b data collected at lower temperatures, see below. The structural models deduced from the D2b data were then used in the analysis of the D1b data.

Simultaneous profile analysis of the XRPD and NPD patterns collected at room temperature gave a satisfactory account of the structures of both compounds. Small amounts of diamagnetic impurities were detected in each sample; 0.8(1) wt % of orthorhombic $LaNbO_4$ in $La_3Ni_2NbO_9$ and 0.4(2) wt % of La_3TaO_7 in $La_3Ni_2TaO_9$. No Bragg peaks attributable to unreacted NiO were observed in either case. The observed and calculated room-temperature XPRD and NPD patterns of $La_3Ni_2NbO_9$ and $La_3Ni_2TaO_9$ are displayed in Figures 1 and 2, respectively. The structural parameters of $La_3Ni_2NbO_9$ and $La_3Ni_2TaO_9$ derived from these analyses are presented in Tables 1 and 2, respectively. In order to achieve a satisfactory fit to the data collected from $La_3Ni_2NbO_9$ it was necessary to include a parameter to model the effect of a small particle size on the shape of the Bragg peaks and, for comparison purposes,

this parameter was also included in refinements of $La_3Ni_2TaO_9$. The ratio of the parameters determined from our X-ray data suggested that the Ta:Nb particle size ratio was 1.67(7):1

SAED patterns of both compounds are shown in Figure 3. The patterns can be indexed using the cell parameters obtained from the XRPD and NPD data. The derived reflection conditions correspond with space group $P2_1/n$. Reflections can be seen in [100] and [001] at *h00, 0k0* and *00l* with respectively *h,k* and *l* odd, which would contradict the $P2_1/n$ symmetry. However, these reflections are due to double diffraction, since they disappear when the sample is tilted around the relevant axes. The cation ordering that occurs over the six-coordinate position is clear from the HR-EDX images in Figure 4. The order is long range, as seen in the HAADF-STEM images of Figure 5. No systematic presence of disordered areas could be found. The different appearance between the HAADF-STEM images of $La_3Ni_2NbO_9$ and $La_3Ni_2TaO_9$ is due to the difference in atomic number *Z* between Ta and Nb: on such images, the brightness of the dots increases with increasing total *Z* of the column. Therefore, the difference between columns with only Ni (Z = 28) or with approximately 1/3 Ni + 2/3Ta ($Z_{average}$ = 58) is larger than the difference between Ni columns and 1/3Ni + 2/3 Nb columns ($Z_{average}$ = 37), giving a clearer alternating contrast at the six-coordinate sites for the Ta-containing sample.

Both materials show the presence of structured diffuse scattering (Figure 6), most probably connected to short range order at the 2*d* position, which is occupied by approximately 1/3 Ni and 2/3 either Ta or Nb. By eye, there is no systematic difference in the shape or intensity of this diffuse scattering between the Nb and Ta containing compounds. To the best of our knowledge, no protocol to quantify diffuse intensities from electron diffraction patterns has yet been developed; a detailed investigation of the precise structural modifications responsible for the diffuse intensity is therefore beyond the scope of the present paper.

The sizes of the particles were analyzed using SEM. As can be clearly seen on Figure S4, the $La_3Ni_2NbO_9$ particles are slightly larger than those of $La_3Ni_2TaO_9$. The sizes were quantified using Digital Micrograph to determine a value for the diameter of the particles, using either the mean diameter along two perpendicular directions or using a spherical particle approximation. The average sizes were in both approximations about 670(30) nm and 580(20) nm for $La_3Ni_2NbO_9$ and $La_3Ni_2TaO_9$, respectively, but for both compounds there is a large range in sizes, varying over several hundred nm (Figure S5).

The temperature dependence of the ZFC and FC molar magnetic susceptibilities of $La_3Ni_2NbO_9$ and $La_3Ni_2TaO_9$ measured in 100 Oe are shown in Figure 7. $\chi^{-1}(T)$ is linear above ~175 K but neither sample behaves as a Curie paramagnet below that temperature. The

effective magnetic moment, μ_{eff}, and the Weiss temperature, θ, derived from fitting the data collected above 200 K to the Curie-Weiss law are listed in Table 3, along with the corresponding parameters for $La_3Ni_2SbO_9$ [2]. The ZFC susceptibility of each compound reaches a maximum at a temperature T_{MAX}, see Table 3, and below this temperature there is a clear difference between the ZFC and FC susceptibilities. The FC susceptibilities measured in 10, 100 and 1000 Oe are shown in Figure 8. Note that χ_{max} is an order of magnitude greater in $La_3Ni_2TaO_9$ and that hysteresis persists somewhat above T_{MAX} in that compound. Furthermore, the susceptibility of $La_3Ni_2TaO_9$ is strongly field dependent at all temperatures below 85 K whereas that of the niobium analogue is essentially independent of field above T_{MAX} and shows a relatively weak field dependence below that temperature. $M(H)$ for each compound is shown in Figure 9 and the values of the coercive field (H_C) and remanent magnetisation (M_R) observed at 5 K are included in Table 3. Although both compounds show their susceptibility maximum below 100 K, $M(H)$ is not a linear function for either compound at 150 K but it is linear for both at 220 K. The deviation from linearity at 150 K is greater in the case of $La_3Ni_2TaO_9$. The temperature and frequency dependence of the ac molar susceptibilities of $La_3Ni_2NbO_9$ and $La_3Ni_2TaO_9$ are shown in Figure 10. In the case of $La_3Ni_2NbO_9$ the temperature of the susceptibility maximum is frequency dependent and the susceptibility is complex below this temperature. The parameter $\Delta T_f/[T_f\Delta(\log \omega)]$ takes a value of 0.0167, indicating that $La_3Ni_2NbO_9$ can be classified as a canonical spin glass. The temperature of the maximum in χ' corresponds closely to T_{MAX} observed in the dc susceptibility. However, the data in Figure 10(b) show anomalous behaviour in $La_3Ni_2TaO_9$ below 85 K, the temperature below which hysteresis is observed in the dc susceptibility and well above T_{MAX}. The ac susceptibility is again complex below the transition temperature, which shows no clear frequency dependence. The two compounds clearly have very different magnetic properties.

No magnetic Bragg peaks were detected in any of the NPD patterns collected below room temperature on D2b or D1b, despite the enhanced counting statistics of the latter. The results of our analysis of the data collected at 5 K on D2b are shown in Figure S1 and the refined structural parameters of $La_3Ni_2NbO_9$ and $La_3Ni_2TaO_9$ at 5 K are listed in Tables 4 and 5, respectively. Some selected bond lengths and angles at room temperature and 5 K are listed in Tables 6 and 7, respectively. To facilitate comparison, the corresponding quantities reported by Battle *et al* for $La_3Ni_2SbO_9$ [2] are also included in these tables. The results of our analyses of NPD data collected on D1b for $5 < T/K < 300$ can be found in Figures S2 and

S3; the structural parameters resulting from the analysis of data collected on D2b at intermediate temperatures are listed in Tables S1, S2 and S3.

The muon asymmetry for $La_3Ni_2B'O_9$ (B'=Sb, Nb, Ta) is plotted in Figure 11 for a representative set of temperatures (data collected at the Swiss Muon Source). For each compound, heavily-damped oscillatory behaviour is found at low temperatures, proving the presence of a static spin system in all three compositions. The heavy damping suggests that the muons experience a range of fields and is consistent with the presence of either long-range or short-range magnetic order. The observed asymmetry at low temperatures is well described by a fitting function of the form $A_1\cos(\gamma_\mu B_\mu t)\exp(-\lambda_1 t)+A_2\exp(-\lambda_2 t)+A_3\exp(-\lambda_3 t)$, where $\gamma_\mu=2\pi\times135.5$ MHz/T is the muon gyromagnetic ratio and λ_i are relaxation rates. The first term models the oscillatory signal and its fitted amplitude A_1 is much larger than those of the non-oscillating terms (A_2 and A_3), signifying that the majority of the muons indeed stop at a site which is directly sensing the static spin system. We attribute the smaller non-oscillatory terms to a combination of muons stopping in regions in which the local field is along the muon polarization direction and muons stopping in the cryostat tails. The exponentials account for temporal fluctuations of the local magnetic field. At higher temperatures a single, non-oscillatory exponentially relaxing component is sufficient to describe the muon asymmetry. The fitted values for the mean local field $B_\mu(T)$ as a function of temperature are presented in Figure 12, and are shown together with fitted curves obtained from the phenomenological relation $B_\mu(T)= B_0(1-(T/T_c)^\alpha)^\beta$. These fitted curves yield values for the transition temperature T_c of 95 K for B'=Sb, 38 K for B'=Nb and 30 K for B'=Ta, and show that $B_\mu(0)$ = 290(10) mT for all three compounds.

Further muon data were obtained on two of the compounds, B'=Sb and Nb, at the EMU muon spectrometer at STFC ISIS. However, the large value of B_μ precludes direct measurement of precession signals at a pulsed muon source such as ISIS where the frequency resolution is more limited. Nevertheless, a critical slowing down of the fluctuations near the transition temperature can be observed when fitting a single exponential with relaxation rate λ to the data. Fitted values for the relaxation rate λ are presented in the inset of Figure 12 and a peak analysis finds the maxima in λ (inversely proportional to the magnetic fluctuation rate) to be in good agreement with the transition temperatures of about 95 K for B'=Sb and 38 K for B'=Nb.

Discussion

Analysis of the X-ray and neutron diffraction data resulted in a structural model similar to that derived previously [2] in the case of $La_3Ni_2SbO_9$. As a consequence of the differences in size and charge of Ni^{2+} and *B*', the Ni^{2+} cations and the pentavalent cations in both $La_3Ni_2NbO_9$ and $La_3Ni_2TaO_9$ order over the six-coordinate sites of the perovskite structure such that the 2*c* site is occupied almost entirely by the former and the 2*d* site by Ni^{2+} and *B*' in an approximately 1:2 ratio; the deviation from the ideal distribution is greater in the niobium-containing compound, although it is lower than that reported in a previous study [3]. The longer bond lengths around the 2*c* site, see Tables 6 and 7, reflect the size difference between the two cation species. The La – O bond lengths and the bond angles within the framework of octahedra are typical of those found in oxide perovskites. The monoclinic structure described above is also consistent with the electron diffraction patterns shown in Figure 3. The HAADF-STEM image of $La_3Ni_2TaO_9$, see Figure 5, demonstrates clearly the cation ordering over the two six-coordinate sites but as a consequence of the reduced contrast, this is not so clear in the image of $La_3Ni_2NbO_9$. However, the EDX map in Figure 4 confirms that, in the selected area, the cation ordering is present. A quantitative analysis of the spot intensities in the columns of cations in Figure 5 did not reveal any extended regions in which the cation ordering was absent, although there were some local fluctuations in both compounds.

The magnetometry data collected on our sample of $La_3Ni_2NbO_9$ are in good agreement with those presented previously by Dey *et al* [12]. Above 35 K the temperature dependence of the susceptibility of $La_3Ni_2NbO_9$, see Figures 7 and 8, is characteristic of a paramagnet with relatively strong intercation interactions. The positive Weiss constant, see Table 3, suggests that a transition to a ferro- or ferrimagnetic phase might occur at low temperatures but below 35 K the susceptibility is actually characteristic of a spin glass. In order to account for similar behaviour in other cation-disordered perovskites it was proposed that the frustration necessary for the formation of a spin glass results from competition between nearest-neighbour and next-nearest-neighbour superexchange interactions that favour the adoption of different magnetic structures [13]. The relative strengths of the different interactions within a particular region of a crystallite will be determined by the local composition. It seems likely that the same factors are involved in the case of $La_3Ni_2NbO_9$, where the random distribution of Ni^{2+} and Nb^{5+} over the 2*d* sites will cause local fluctuations in composition. The absence of magnetic Bragg scattering in the neutron diffraction data can then be explained by postulating that a particular pattern of cation ordering is never maintained over distances long enough to allow the development of islands of coherent magnetic order that can be detected

by neutron diffraction. However, the diffuse scattering apparent in Figure 6 suggests that cation ordering is present over short distances. We have previously [7] shown that in the case of $La_3Ni_2SbO_9$ the alignment of small ferrimagnetic domains is responsible for the observation of a large magnetisation in an applied magnetic field and the *M(H)* behaviour of $La_3Ni_2NbO_9$, see Figure 9, can be explained in the same way. The observation of oscillations in the μSR data below 35 K, see Figures 12 and 13, is consistent with this explanation. The presence of oscillations proves that static spins are present at low temperatures but their rapid damping suggests that they may be ordered only in relatively small regions.

Like $La_3Ni_2NbO_9$, $La_3Ni_2TaO_9$ has a relatively large and positive Weiss constant in the paramagnetic region. However, below ~100 K $\chi(T)$ behaves in a manner that is reminiscent of the relaxor ferromagnet $La_3Ni_2SbO_9$ rather than the niobium-containing composition. In common with the latter, the dc susceptibility measured in 100 Oe has a clear maximum at T_{MAX} ~35 K but the magnitude of the susceptibility is an order of magnitude greater in $La_3Ni_2TaO_9$. Furthermore, hysteresis is clearly apparent in $\chi(T)$ between T_{MAX} and ~80 K whereas none was detected in the data collected on $La_3Ni_2NbO_9$ above 30 K. The temperature dependence of the ac susceptibility is also markedly different, see Figure 10. The frequency dependence of the real component and the appearance of an imaginary component, taken together with the presence of hysteresis in the dc data, suggest that magnetised domains are present below ~80 K. The coercive field is smaller in $La_3Ni_2TaO_9$ than in $La_3Ni_2NbO_9$, suggesting that the domain size is different in the two materials. However, the μSR data in Figure 13 suggest that the spins only become static on a microsecond timescale below 35 K. In order to account for these data we propose that extensive short-range magnetic ordering, resulting in the formation of relatively-large rapidly-relaxing ferrimagnetic clusters is well-established at ~80 K in $La_3Ni_2TaO_9$. On further cooling the larger clusters become blocked, giving rise to hysteresis in *[6]*and on cooling below 35 K the spins become static, but still in clusters too small to be detected in a neutron diffraction experiment. In the future we intend to study this short-range ordering using the appropriate neutron scattering techniques but for the present we are unable to describe the phenomenon more fully.

The differences in the magnetic behaviours of $La_3Ni_2NbO_9$, $La_3Ni_2TaO_9$ and $La_3Ni_2SbO_9$ are striking, given that they are apparently isostuctural compounds and the changes in chemical composition along the series do not involve the magnetic species. Changes in the chemical bonding brought about by the differences in the electronic structure of the diamagnetic, pentavalent cation are one possible cause. Comparative studies of the perovskites Sr_2NiWO_6 and Sr_2NiTeO_6 [8, 9] and other pairs of d^0 and d^{10} compounds have shown that the magnetic

structure adopted at low temperatures is partly dependent on whether the diamagnetic cation on the six-coordinate sites has empty *d* orbitals available to take part in the superexchange interactions. Thus it is not surprising that $La_3Ni_2SbO_9$ and $La_3Ni_2NbO_9$ behave differently but $La_3Ni_2TaO_9$ would be expected to lie closer to the latter rather than the former. We must therefore look for structural variations in order to explain the behaviour of these three compounds.

One factor that could be important is the extent to which the B'^{5+} and Ni^{2+} cations order over the six-coordinate sites. Our neutron diffraction experiments determine the average site occupancies across the crystallites; they do not identify local deviations from the mean distribution. When judged on the former length scale, the degree of ordering increases in the sequence Nb < Ta < Sb but the differences are small and the 2*d* site is still 96.4(7) % occupied by Ni^{2+} in the most heavily disordered niobium-containing sample. It therefore seems likely that in order to understand the magnetic behaviour we must look at the structures over shorter length scales that are not probed in a neutron diffraction experiment.

In all our recent work on perovskites, TEM has been used to look for local anomalies in the cation-ordering pattern. In the case of $La_3Ni_2SbO_9$ we found evidence for a breakdown in the ordering and we proposed that the disordered regions served as magnetic domain walls between neighbouring ordered regions and this explanation caused us to label $La_3Ni_2SbO_9$ as a relaxor ferromagnet. No comparable features have been observed in our subsequent TEM studies of $CaLn_2Ni_2WO_9$ (*Ln* = La, Pr, Nd) [6] and $La_3Ni_2NbO_9$ which all show spin-glass-like behaviour at low temperatures. However, nor have they been observed in $La_3Ni_2TaO_9$, despite the fact that the magnetic behaviour of that compound is somewhat similar to that of $La_3Ni_2SbO_9$. The only indications of a difference between the microstructure of $La_3Ni_2TaO_9$ and that of $La_3Ni_2NbO_9$ are the difference in the coercive fields derived from $M(H)$ and the apparent inconsistency in the relative particle size as determined by SEM and neutron diffraction. The analysis of the neutron diffraction data on $La_3Ni_2NbO_9$ required the use of a parameter that takes account of a small particle size. The observation of a small particle size in $La_3Ni_2NbO_9$ is consistent with the findings of Inprasit *et al* [14] but, interestingly, our subsequent SEM measurements found that the particle size in our sample of $La_3Ni_2NbO_9$ was actually greater than that in our sample of $La_3Ni_2TaO_9$.

The complexity of the microstructure in this family of compounds has been established previously by the observation of disordered regions in $La_3Ni_2SbO_9$ and the coexistence of spin-glass behaviour and long-range magnetic order in $SrLa_2Ni_2TeO_9$ [5]. One self-consistent explanation of our most recent observations is that the niobium-containing sample typically

consists of relatively-large particles which contain multiple relatively-small, structurally-coherent domains whereas $La_3Ni_2TaO_9$ consists of smaller particles made up of a single, relatively-large structural domain. This is the most viable explanation for the difference in the properties of the two compounds.

Conclusion

$La_3Ni_2SbO_9$, $La_3Ni_2NbO_9$ and $La_3Ni_2TaO_9$ all adopt the same monoclinic, perovskite-like structure and show similar degrees of cation ordering over the six-coordinate sites. However, marked differences are apparent in their magnetic properties. Surprisingly, the contrast between the Sb^{5+} (d^{10}) and Ta^{5+}(d^0) compounds is less than that between those containing Ta^{5+} and Nb^{5+} (d^0). We propose that the origin of this anomaly lies in the microstructure of our samples. Finally, we note that the presence of strong diffuse scattering, see Figure 6, clearly shows that local structural variations are present in these materials and we shall endeavour to develop a quantitative interpretation of these data in the future.

Acknowledgments

We thank EPSRC for funding through grants EP/M0189541 and EP/N023803. CMC thanks the Croucher Foundation and Oxford University for a graduate scholarship. We are grateful E. Suard for experimental assistance at ILL.

References

[1] M.T. Anderson, K.B. Greenwood, G.A. Taylor, K.R. Poeppelmeier, *Progress in Solid State Chemistry* 22 (1993) 197.
[2] P.D. Battle, S.I. Evers, E.C. Hunter, M. Westwood, *Inorg. Chem.* 52 (2013) 6648.
[3] J.R. Tolchard, M.L. Fontaine, T. Grande, *Acta Crystallographica Section C-Crystal Structure Communications* 65 (2009) I11-I13.
[4] E.C. Hunter, P.D. Battle, R. Paria Sena, J. Hadermann, *J. Solid State Chem.* 248 (2017) 96-103.
[5] R. Paria Sena, J. Hadermann, C.M. Chin, E.C. Hunter, P.D. Battle, *Journal of Solid State Chemistry* 243 (2016) 304-311.
[6] C.M. Chin, R. Paria Sena, E.C. Hunter, J. Hadermann, P.D. Battle, *Journal of Solid State Chemistry* 251 (2017) 224-232.
[7] P.D. Battle, M. Avdeev, J. Hadermann, *J. Solid State Chem.* 220 (2014) 163.
[8] D. Iwanaga, Y. Inaguma, M. Itoh, *Mater. Res. Bull.* 35 (2000) 449.
[9] Y.H. Xu, S.S. Liu, N.R. Qu, Y.L. Cui, Q.Q. Gao, R.N. Chen, J. Wang, F.M. Gao, X.F. Hao, *Journal of Physics-Condensed Matter* 29 (2017).
[10] H.M. Rietveld, *Journal of Applied Crystallography* 2 (1969) 65 - 71.

[11] A.C. Larson, R.B. von-Dreele *General Structure Analysis System (GSAS)* Los Alamos National Laboratories LAUR 86-748 1994
[12] K. Dey, A. Indra, D. De, S. Majumdar, S. Giri, *Acs Applied Materials & Interfaces* 8 (2016) 12901-12907.
[13] E.J. Cussen, J.F. Vente, P.D. Battle, T. Gibb, *Journal of Materials Chemistry* 7 (1997) 459.
[14] T. Inprasit, S. Wongkasemjit, P. Limthongkul, S.J. Skinner, *Materials Letters* 162 (2016) 37-39.

Figure Captions

Figure 1 Observed (red crosses), calculated (green line) and difference (purple) (a) XPRD and (b) NPD profiles of $La_3Ni_2NbO_9$ collected at room temperature. Reflection markers are shown for $LaNbO_4$ (green) and $La_3Ni_2NbO_9$ (black).

Figure 2 Observed (red crosses), calculated (green line) and difference (purple) (a) XPRD and (b) NPD profiles of $La_3Ni_2TaO_9$ collected at room temperature. Reflection markers are shown for La_3TaO_7 (cyan) and $La_3Ni_2TaO_9$ (black).

Figure 3 Representative SAED patterns of the main zones of $La_3Ni_2TaO_9$ (left column) and $La_3Ni_2NbO_9$ (right column).

Figure 4 High resolution EDX maps along [010], showing the distribution of the different elements within the unit cells of $La_3Ni_2TaO_9$ (top row) and $La_3Ni_2NbO_9$ (bottom row).

Figure 5 HAADF-STEM images of the most informative zone [100] of $La_3Ni_2TaO_9$ (left) and $La_3Ni_2NbO_9$ (right). An overlay of the model is shown, using the same colour scheme as the high resolution EDX maps of Figure 4, i.e. red is La, green is Ni and blue is Ta or Nb.

Figure 6 SAED patterns along the [100] zones of $La_3Ni_2TaO_9$ (left) and $La_3Ni_2NbO_9$ (right), showing clear structured diffuse scattering. The patterns are tilted out of zone to increase the visibility of the diffuse scattering.

Figure 7 The ZFC and FC dc molar susceptibility and (inset) inverse susceptibility of (a) $La_3Ni_2NbO_9$ and (b) $La_3Ni_2TaO_9$ measured in 100 Oe as a function of temperature.

Figure 8 The FC dc molar susceptibility of (a) $La_3Ni_2NbO_9$ and (b) $La_3Ni_2TaO_9$ measured in 10, 100 and 1000 Oe as a function of temperature.

Figure 9 The magnetisation per formula unit as a function of magnetic field of (a) $La_3Ni_2NbO_9$ and (b) $La_3Ni_2TaO_9$ at 5 (blue), 150 (red) and 220 (green) K.

Figure 10 The real and imaginary components of the ac susceptibility of (a) $La_3Ni_2NbO_9$ and (b) $La_3Ni_2TaO_9$ as a function of temperature measured at 1 (red), 10 (green) and 100 (blue) Hz.

Figure 11 Muon asymmetry of $La_3Ni_2B'O_9$ (*B'*=Sb, Nb, Ta) measured at the General Purpose Spectrometer (GPS) at the Swiss Muon Source for representative temperatures: well below, slightly above and well above T_c. The solid lines represent the curves fitted using the formulae described in the main text.

Figure 12 Mean local field measured at the muon site as extracted from the muon precession signals. The solid lines are obtained by fitting a phenomenological order parameter equation: $B_\mu(T)=B_0(1-(T/T_c)^\alpha)^\beta$. The inset shows the relaxation rates obtained the EMU spectrometer at ISIS. The peaks in the relaxation rates due to critical slowing down near T_c are in good agreement with the values of T_c obtained from the fits to $B_\mu(T)$.

Table 1. Structural parameters of $La_3Ni_2NbO_9$ at room temperature.

Atom	Site	*x*	*y*	*z*	U_{iso} /Å^2	Occupancy
La	4*e*	0.4921(3)	0.4610(1)	0.2501(3)	0.0195(2)	1
Ni/Nb1	2*c*	0	½	0	0.0032(1)	Ni: 0.964(7) Nb: 0.036(7)
Ni/Nb2	2*d*	½	0	0	0.0032(1)	Ni: 0.369(7) Nb: 0.631(7)
O1	4*e*	0.7912(9)	0.7965(7)	–0.0366(5)	0.0059(10)	1
O2	4*e*	0.7119(9)	0.2835(7)	–0.0472(5)	0.0087(10)	1
O3	4*e*	0.5766(3)	0.0168(3)	0.2499(11)	0.0121(3)	1

XRPD: R_{wp} = 7.62 %, R_p = 5.75 %

NPD: R_{wp} = 4.56 %, R_p = 3.51 %

Total: R_{wp} = 6.25 %, R_p = 5.54 %, χ^2 = 2.293

Space group $P2_1/n$: a = 5.5865(1) Å, b = 5.6400(1) Å, c = 7.9165(1) Å, β = 90.012(5) °.

Table 2. Structural parameters of $La_3Ni_2TaO_9$ at room temperature.

Atom	Site	*x*	*y*	*z*	U_{iso} /Å^2	Occupancy
La	4*e*	0.4924(3)	0.4613(1)	0.2507(2)	0.0224(2)	1
Ni/Ta1	2*c*	0	½	0	0.0048(1)	Ni: 0.982(1) Ta: 0.018(1)
Ni/Ta2	2*d*	½	0	0	0.0048(1)	Ni: 0.351(1) Ta: 0.649(1)
O1	4*e*	0.7886(7)	0.7950(6)	–0.0374(5)	0.0041(8)	1
O2	4*e*	0.7093(8)	0.2851(7)	–0.0469(5)	0.0148(11)	1
O3	4*e*	0.5769(3)	0.0172(3)	0.2518(8)	0.0132(3)	1

XRPD: R_{wp} = 6.46 %, R_p = 4.86 %

NPD: R_{wp} = 4.72 %, R_p = 3.58 %

Total: R_{wp} = 5.76 %, R_p = 4.77%, χ^2 = 2.317

Space group $P2_1/n$: a = 5.5902(1) Å, b = 5.6407(1) Å, c = 7.9222(1) Å, β = 90.034(3) °.

Table 3. Magnetic parameters of $La_3Ni_2B'O_9$ (*B'* = Sb/Nb/Ta).

Composition	μ_{eff} / μ_B	θ / K	M_R / μ_B	H_C / kOe	T_{MAX} / K
$La_3Ni_2SbO_9$	2.2(1)	+159	0.5	0.5	105
$La_3Ni_2NbO_9$	2.12(1)	+137(3)	0.1	1.3	29
$La_3Ni_2TaO_9$	2.15(1)	+144(2)	0.2	0.6	35

Table 4. Structural parameters of $La_3Ni_2NbO_9$ at 5 K.

Atom	Site	*x*	*y*	*z*	U_{iso} /Å^2	Occupancy
La	4*e*	0.4918(5)	0.4588(2)	0.2503(12)	0.0140(3)	1
Ni/Nb1	2*c*	0	½	0	0.00182)	Ni: 0.964(7) Nb: 0.036(7)
Ni/Nb2	2*d*	½	0	0	0.0018(2)	Ni: 0.369(7) Nb: 0.631(7)
O1	4*e*	0.7920(11)	0.7969(10)	–0.0383(7)	0.0012(12)	1
O2	4*e*	0.7119(13)	0.2835(11)	–0.0464(8)	0.0084(15)	1
O3	4*e*	0.5786(4)	0.0174(4)	0.2517(14)	0.0086(5)	1

R_{wp} = 4.72 %, R_p = 3.59 %, χ^2 = 4.618

Space group $P2_1/n$: *a* = 5.5755(1) Å, *b* = 5.6383(1) Å, *c* = 7.9029(2) Å, β = 90.024(9) °.

Table 5. Structural parameters of $La_3Ni_2TaO_9$ at 5 K.

Atom	Site	*x*	*y*	*z*	U_{iso} /Å^2	Occupancy
La	4*e*	0.4919(5)	0.4597(2)	0.2498(12)	0.0143(3)	1
Ni/Ta1	2*c*	0	½	0	0.0012(2)	Ni: 0.982(1) Ta: 0.018(1)
Ni/Ta2	2*d*	½	0	0	0.0012(2)	Ni: 0.351(1) Ta: 0.649(1)
O1	4*e*	0.7896(11)	0.7978(10)	–0.0386(7)	0.0018(13)	1
O2	4*e*	0.7096(12)	0.2835(10)	–0.0462(8)	0.0062(15)	1
O3	4*e*	0.5781(5)	0.0180(4)	0.2510(11)	0.0081(5)	1

NPD: R_{wp} = 4.60 %, R_p = 3.66 %, χ^2 = 3.350

Space group $P2_1/n$: a = 5.5782(2) Å, b = 5.6372(2) Å, c = 7.9067(2) Å, β = 90.064(6) °.

Table 6. Selected bond lengths (Å) and angles (°) in $La_3Ni_2B'O_9$ (*B'* = Sb, Nb or Ta) at RT.

	$La_3Ni_2SbO_9$	$La_3Ni_2NbO_9$	$La_3Ni_2TaO_9$
La–O1	2.815(9)	2.733(4)	2.745(4)
La–O1	2.687(7)	2.733(4)	2.721(4)
La–O1	2.384(8)	2.446(4)	2.452(4)
La–O2	2.799(9)	2.838(5)	2.831(4)
La–O2	2.478(8)	2.440(5)	2.433(4)
La–O2	2.686(8)	2.632(5)	2.648(5)
La–O3	2.561(2)	2.549(2)	2.549(2)
La–O3	2.448(4)	2.430(2)	2.429(2)
2*c* – O1	2.094(5)×2	2.059(4)×2	2.062(3)×2
2*c* – O2	2.055(6)×2	2.054(4)×2	2.061(4)×2
2*c* – O3	2.071(10)×2	2.028(9)×2	2.016(6)×2
2*d* – O1	2.007(6)×2	2.012(4)×2	2.007(3)×2
2*d* – O2	2.012(6)×2	2.024(4)×2	2.023(4)×2
2*d* – O3	1.993(10)×2	2.026(9)×2	2.042(6)×2
O1 –2*c*–O2	89.7(3)×2	89.2(3)×2	89.8(2)×2
O1– 2*c* –O3	88.9(2)×2	88.8(1)×2	88.8(1)×2
O2 – 2*c* –O3	89.4(2)×2	87.7(1)×2	88.0(1)×2
O1 – 2*d* – O2	87.6(3)×2	87.2(3)×2	88.1(2)×2
O1 – 2*d* – O3	87.8(2)×2	89.8(1)×2	89.8(1)×2
O2 – 2*d* – O3	89.2(2)×2	88.9(1)×2	88.9(1)×2
2*c* – O1 – 2*d*	151.62(1)	154.3(2)	154.7(2)
2*c* – O2 – 2*d*	155.62(1)	153.4(2)	152.9(2)
2*c* – O3 – 2*d*	155.12(1)	155.04(9)	154.9(1)

Table 7. Selected bond lengths (Å) and angles (°) in $La_3Ni_2B'O_9$ (*B'* = Sb, Nb or Ta) at 5 K.

	$La_3Ni_2SbO_9$	$La_3Ni_2NbO_9$	$La_3Ni_2TaO_9$
La–O1	2.833(8)	2.732(10)	2.743(10)
La–O1	2.658(7)	2.718(8)	2.712(9)
La–O1	2.401(8)	2.435(9)	2.439(9)
La–O2	2.767(9)	2.826(10)	2.819(10)
La–O2	2.463(8)	2..449(9)	2.438(9)
La–O2	2.693(8)	2.624(9)	2.639(9)
La–O3	2.545(3)	2.535(2)	2.536(3)
La–O3	2.463(4)	2.418(3)	2.421(4)
2*c* – O1	2.088(5)×2	2.059(5)×2	2.070(5)×2
2*c* – O2	2.050(6)×2	2.050(6)×2	2.060(5)×2
2*c* – O3	2.036(10)×2	2.013(11)×2	2.020(9)×2
2*d* – O1	2.011(5)×2	2.014(6)×2	2.001(5)×2
2*d* – O2	2.012(5)×2	2.021(6)×2	2.014(6)×2
2*d* – O3	2.025(10)×2	2.039(11)×2	2.034(9)×2
O1 –2*c*–O2	89.8(3)×2	89.0(4)×2	89.5(3)×2
O1– 2*c* –O3	89.0(2)×2	88.9(2)×2	88.9(2)×2
O2 – 2*c* –O3	89.7(2)×2	88.1(2)×2	88.1(2)×2
O1 – 2*d* – O2	87.5(3)×2	87.1(4)×2	87.4(4)×2
O1 – 2*d* – O3	87.6(2)×2	90.0(2)×2	89.7(2)×2
O2 – 2*d* – O3	89.2(2)×2	89.2(2)×2	89.2(2)×2
2*c* – O1 – 2*d*	151.3(3)	153.6(3)	153.8(3)
2*c* – O2 – 2*d*	155.7(3)	153.7(4)	153.4(4)
2*c* – O3 – 2*d*	154.7(2)	154.4(1)	154.5(1)

(a)

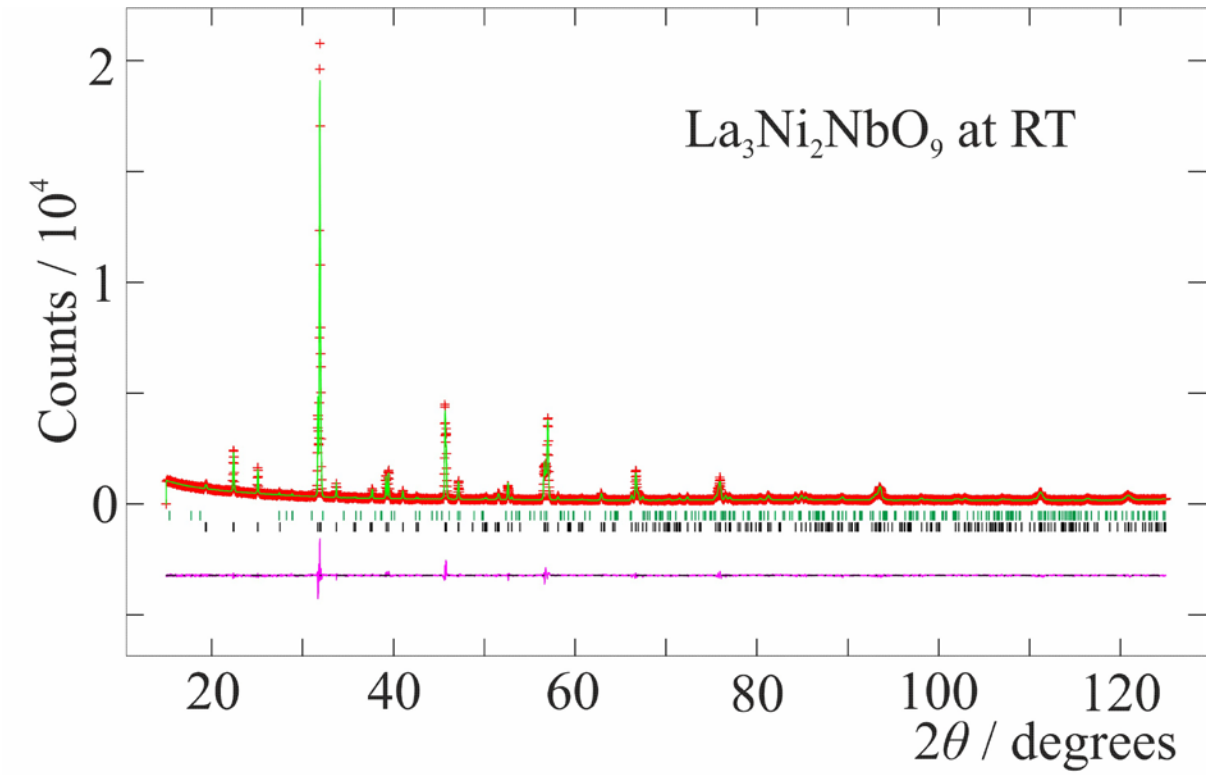
La3Ni2NbO9 at RT
Counts / 10^4
2θ / degrees

(b)

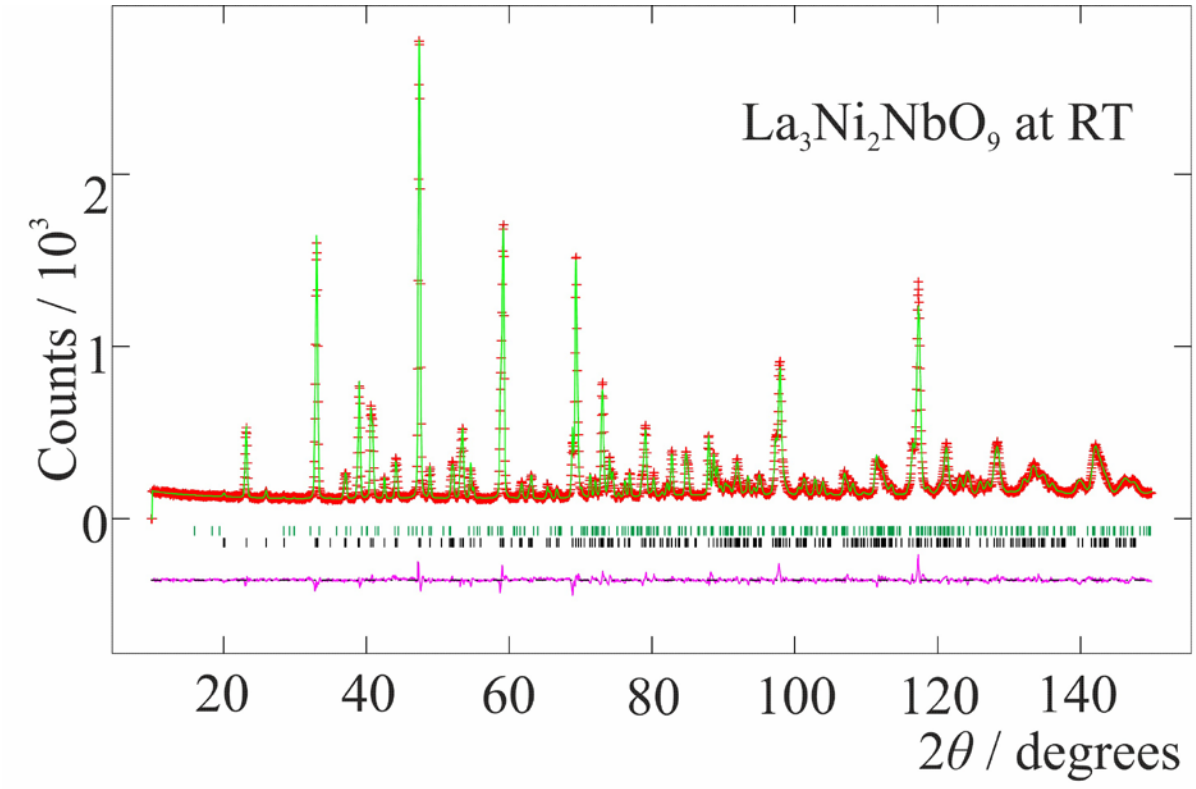
La3Ni2NbO9 at RT
Counts / 10^3
2θ / degrees

Figure 1

(a)

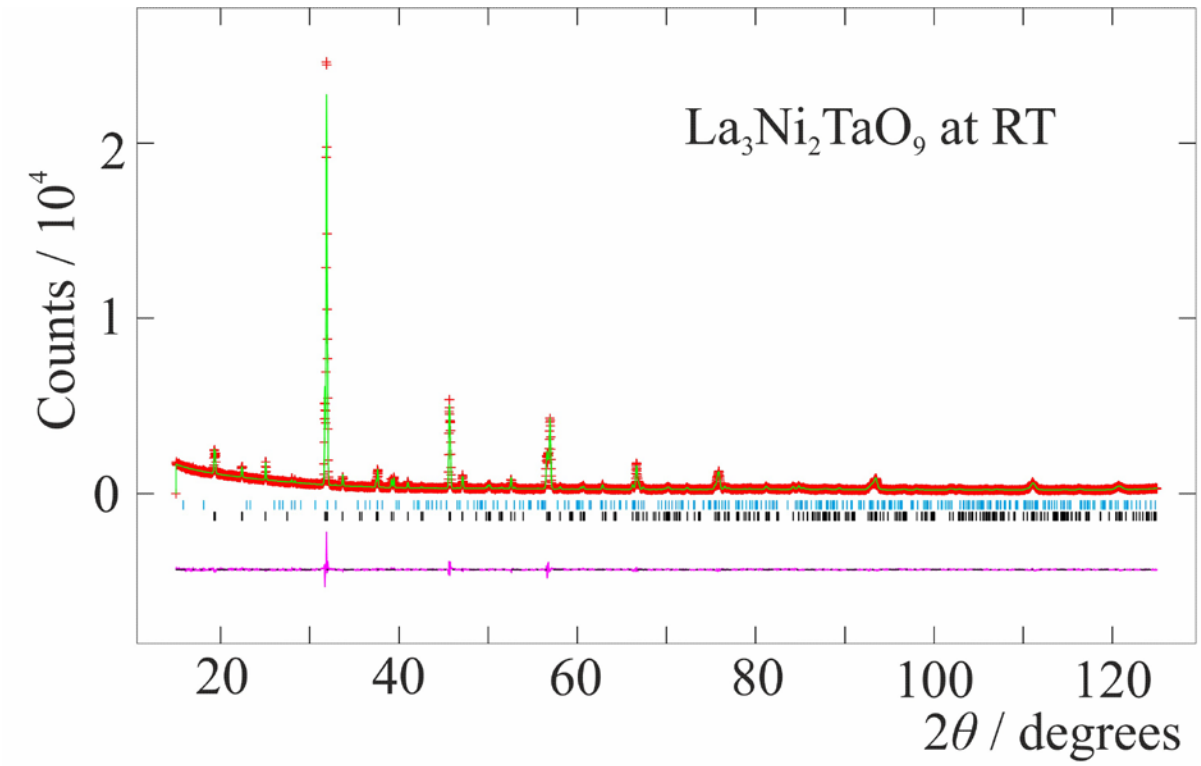
La3Ni2TaO9 at RT
Counts / 10^4
2
1
0
20
40
60
80
100
120
2θ / degrees

(b)

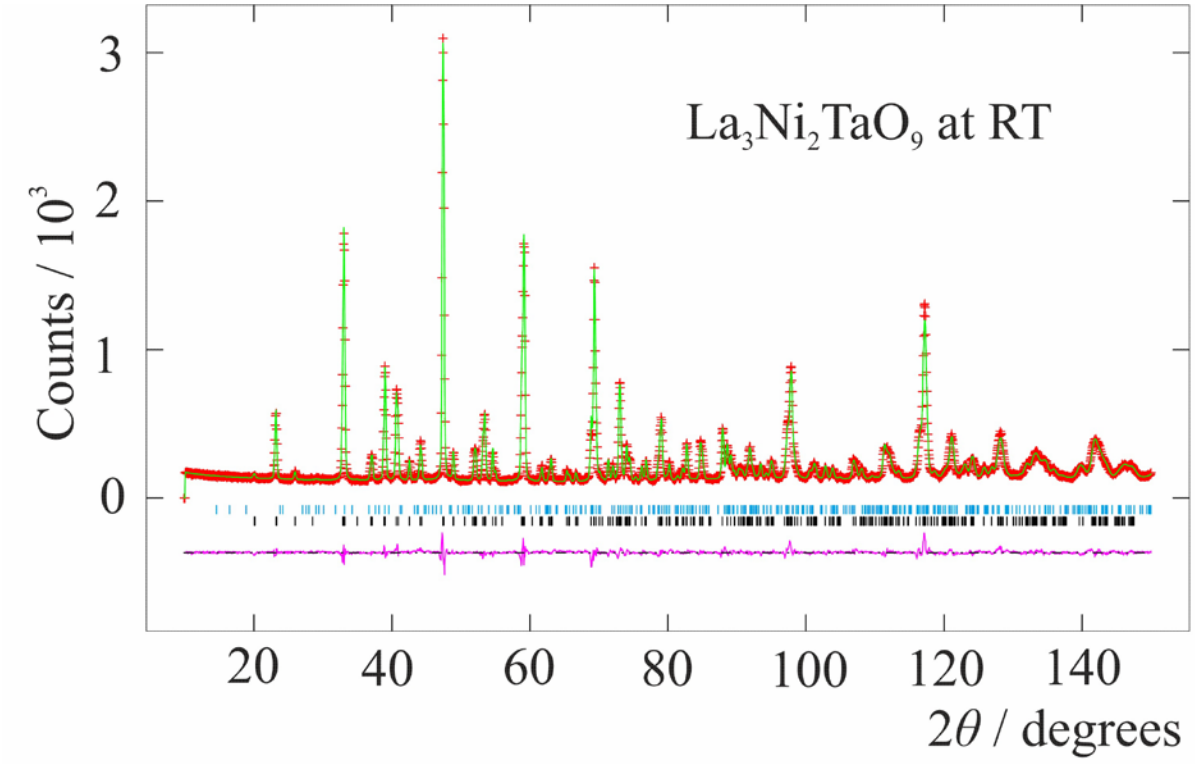
La3Ni2TaO9 at RT
Counts / 10^3
3
2
1
0
20
40
60
80
100
120
140
2θ / degrees

Figure 2

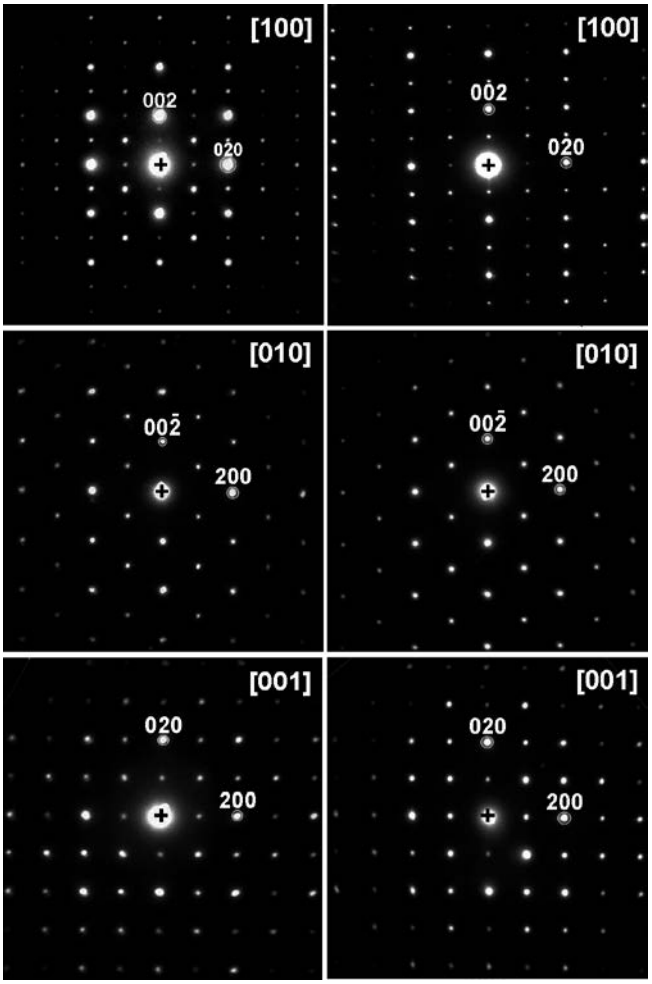
[100]
002
020
[100]
002
020
[010]
00$\bar{2}$
200
[010]
00$\bar{2}$
200
[001]
020
200
[001]
020
200

Figure 3

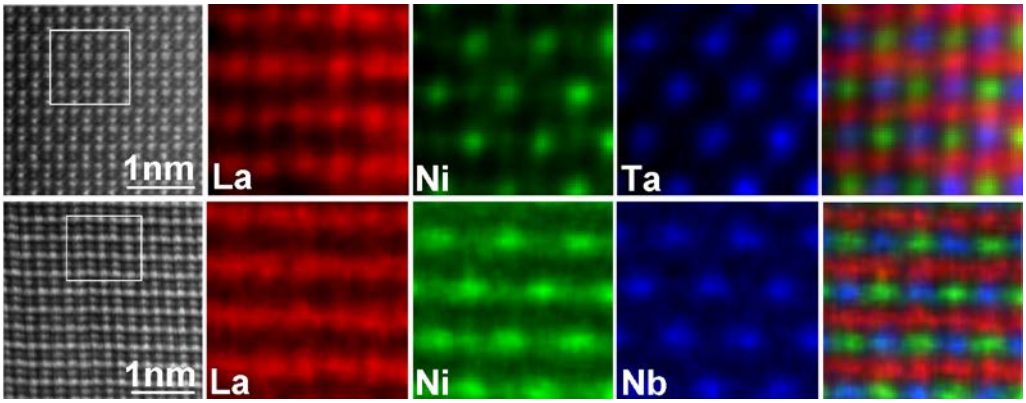

Figure 4

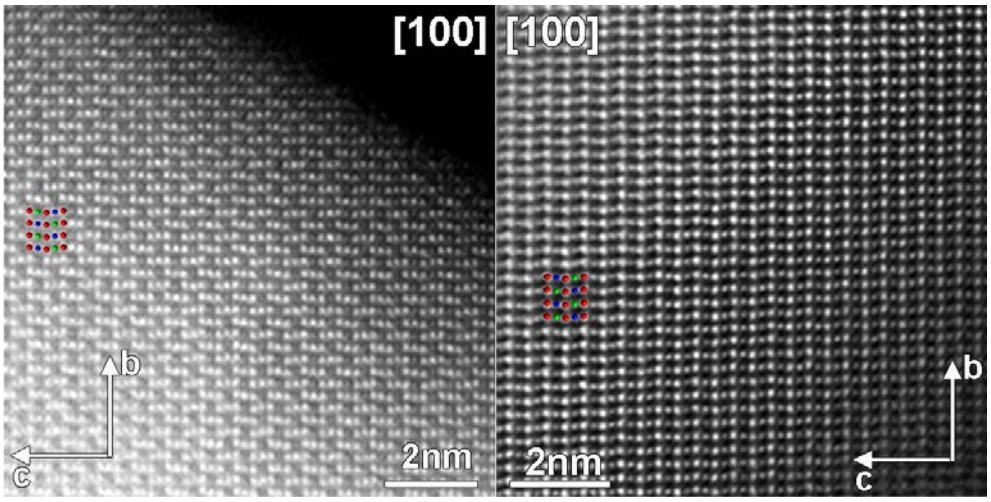

Figure 5

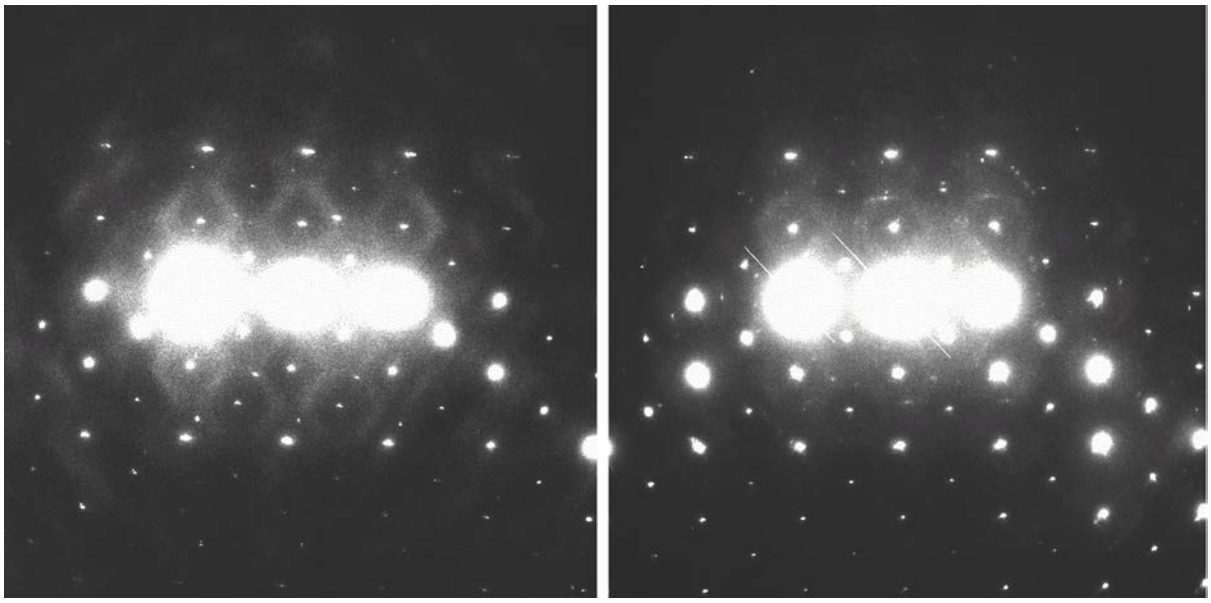

Figure 6

(a)

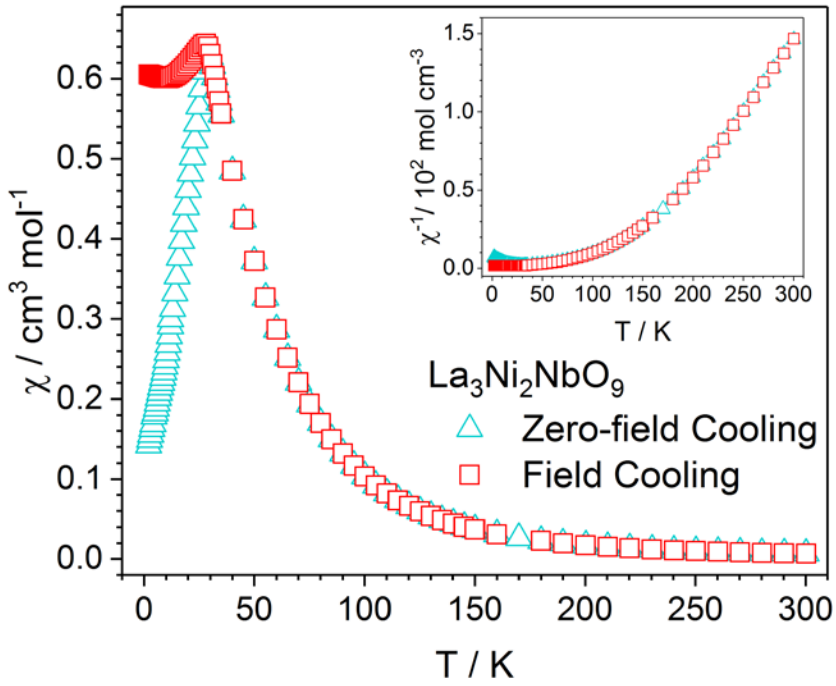
χ / cm3 mol-1
T / K
χ-1 / 102 mol cm-3
La3Ni2NbO9
Zero-field Cooling
Field Cooling

(b)

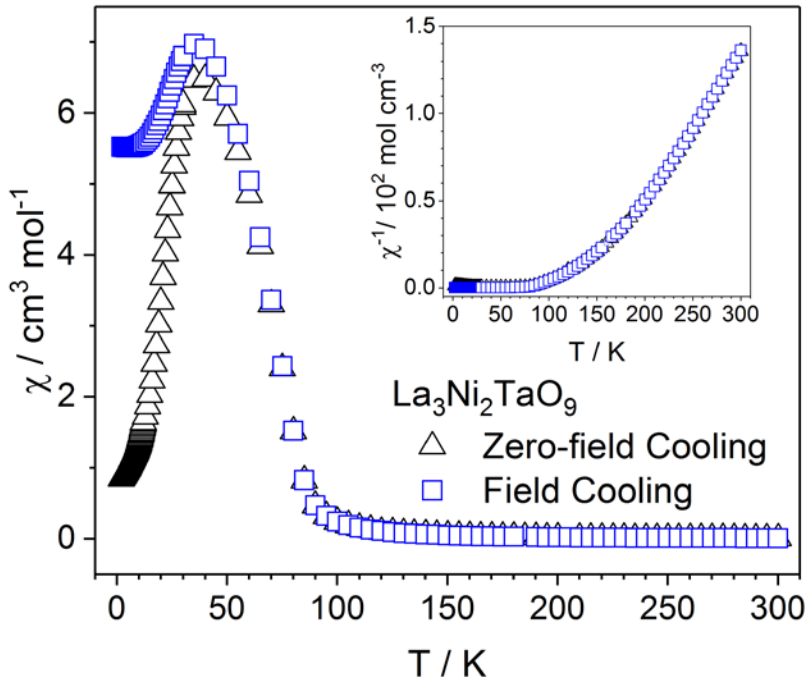
χ / cm3 mol-1
T / K
χ-1 / 102 mol cm-3
La3Ni2TaO9
Zero-field Cooling
Field Cooling

Figure 7

(a)

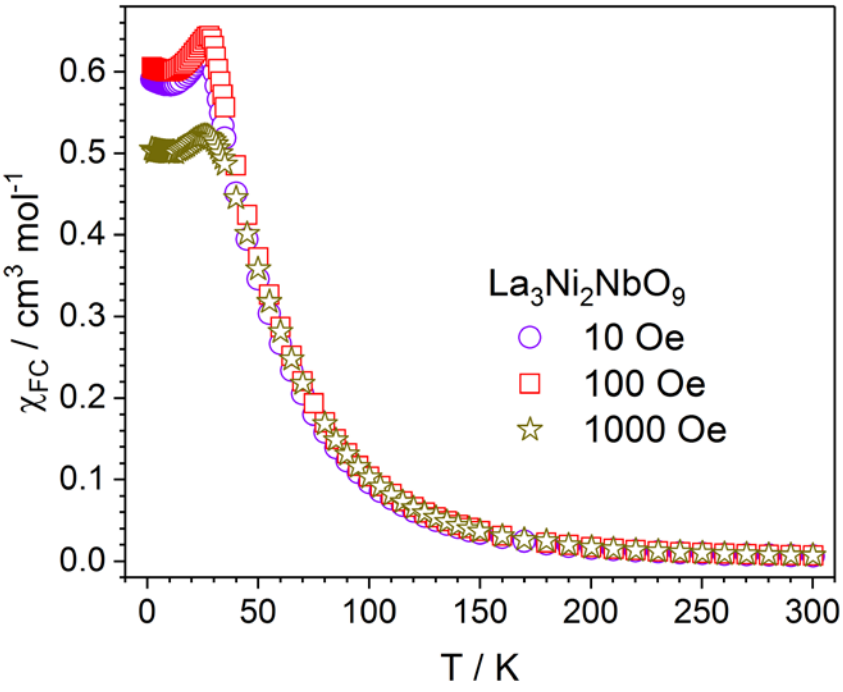
0.6
0.5
0.4
0.3
0.2
0.1
0.0
χFC / cm3 mol-1
La3Ni2NbO9
10 Oe
100 Oe
1000 Oe
0
50
100
150
200
250
300
T / K

(b)

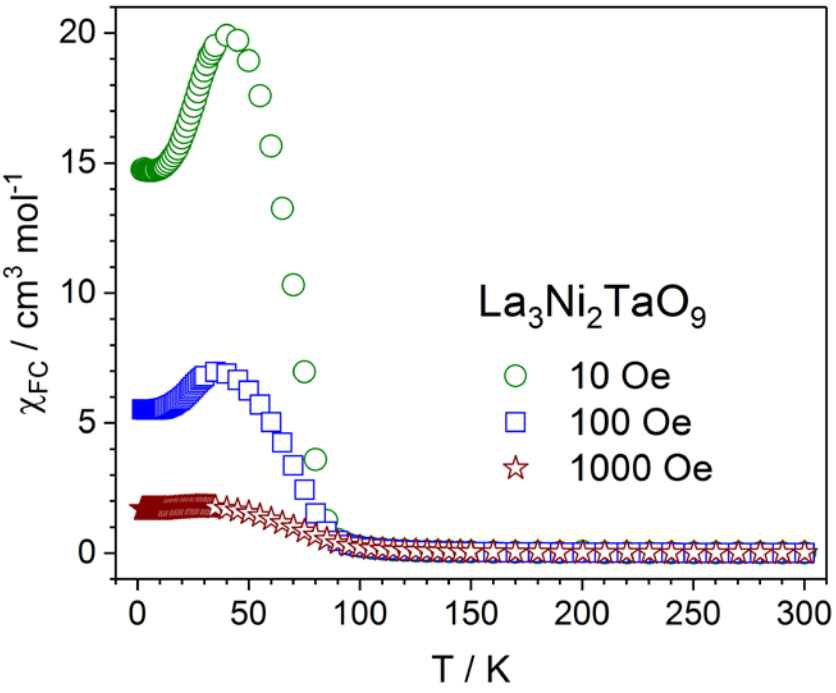
20
15
10
5
0
χFC / cm3 mol-1
La3Ni2TaO9
10 Oe
100 Oe
1000 Oe
0
50
100
150
200
250
300
T / K

Figure 8

(a)

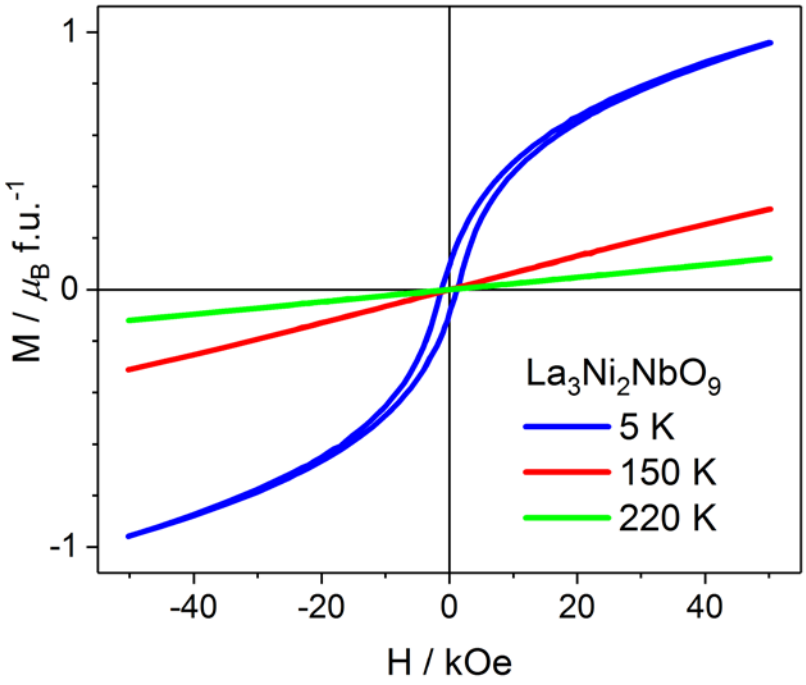
1
0
-1
M / μ_B f.u.$^{-1}$
-40
-20
0
20
40
H / kOe
$La_3Ni_2NbO_9$
5 K
150 K
220 K

(b)

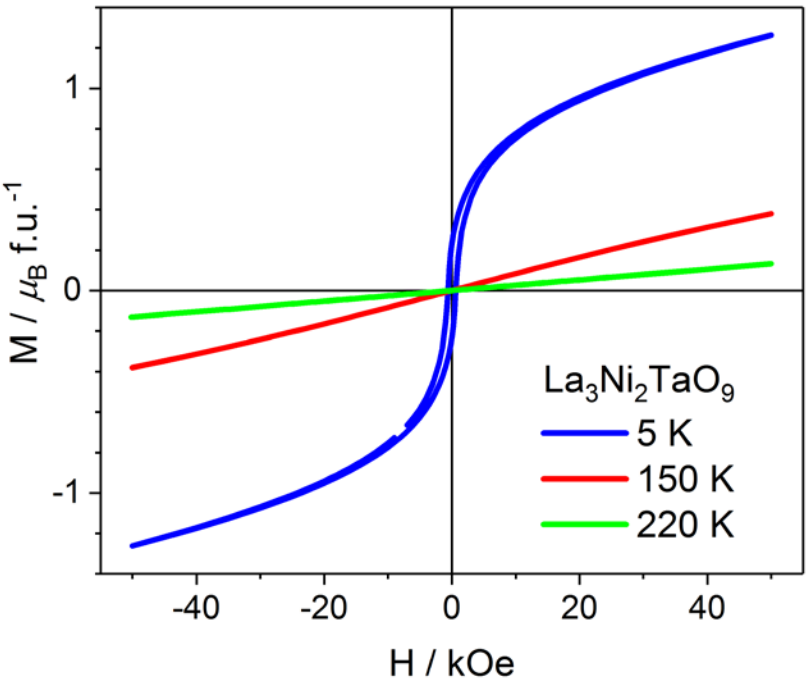
1
0
-1
M / μ_B f.u.$^{-1}$
-40
-20
0
20
40
H / kOe
$La_3Ni_2TaO_9$
5 K
150 K
220 K

Figure 9

(a)

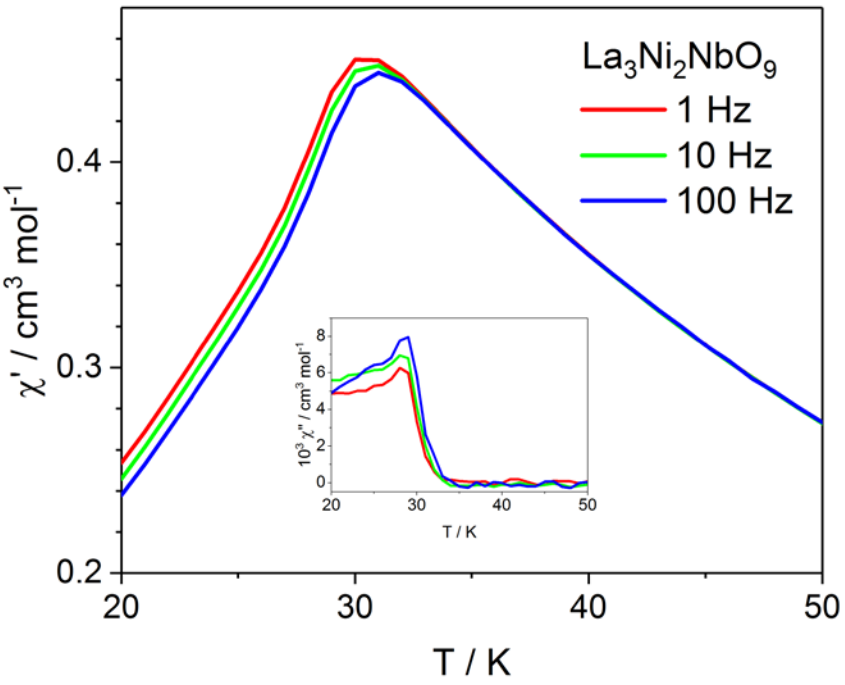
La3Ni2NbO9
1 Hz
10 Hz
100 Hz
χ' / cm3 mol-1
T / K
10-3 χ'' / cm3 mol-1

(b)

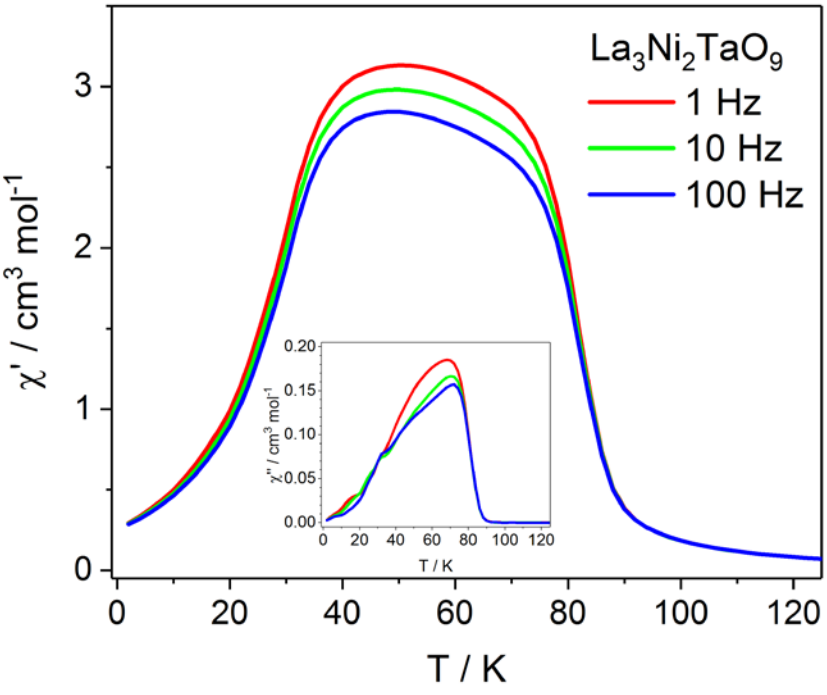
La3Ni2TaO9
1 Hz
10 Hz
100 Hz
χ' / cm3 mol-1
T / K
χ'' / cm3 mol-1

Figure 10

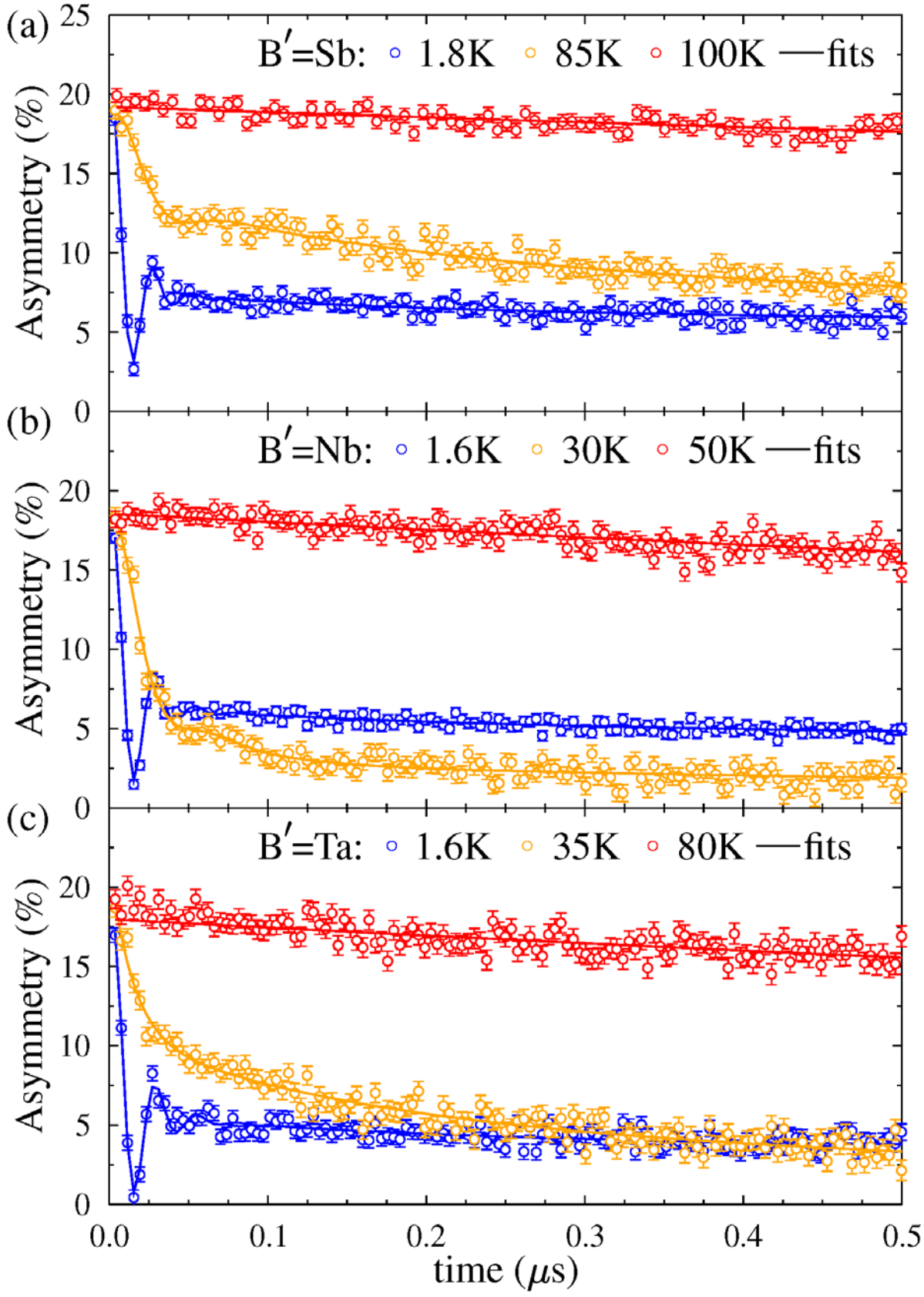
(a)
B′=Sb: 1.8K 85K 100K —fits
Asymmetry (%)
(b)
B′=Nb: 1.6K 30K 50K —fits
Asymmetry (%)
(c)
B′=Ta: 1.6K 35K 80K —fits
Asymmetry (%)
0 5 10 15 20 25
0.0 0.1 0.2 0.3 0.4 0.5
time (μs)

Figure 11

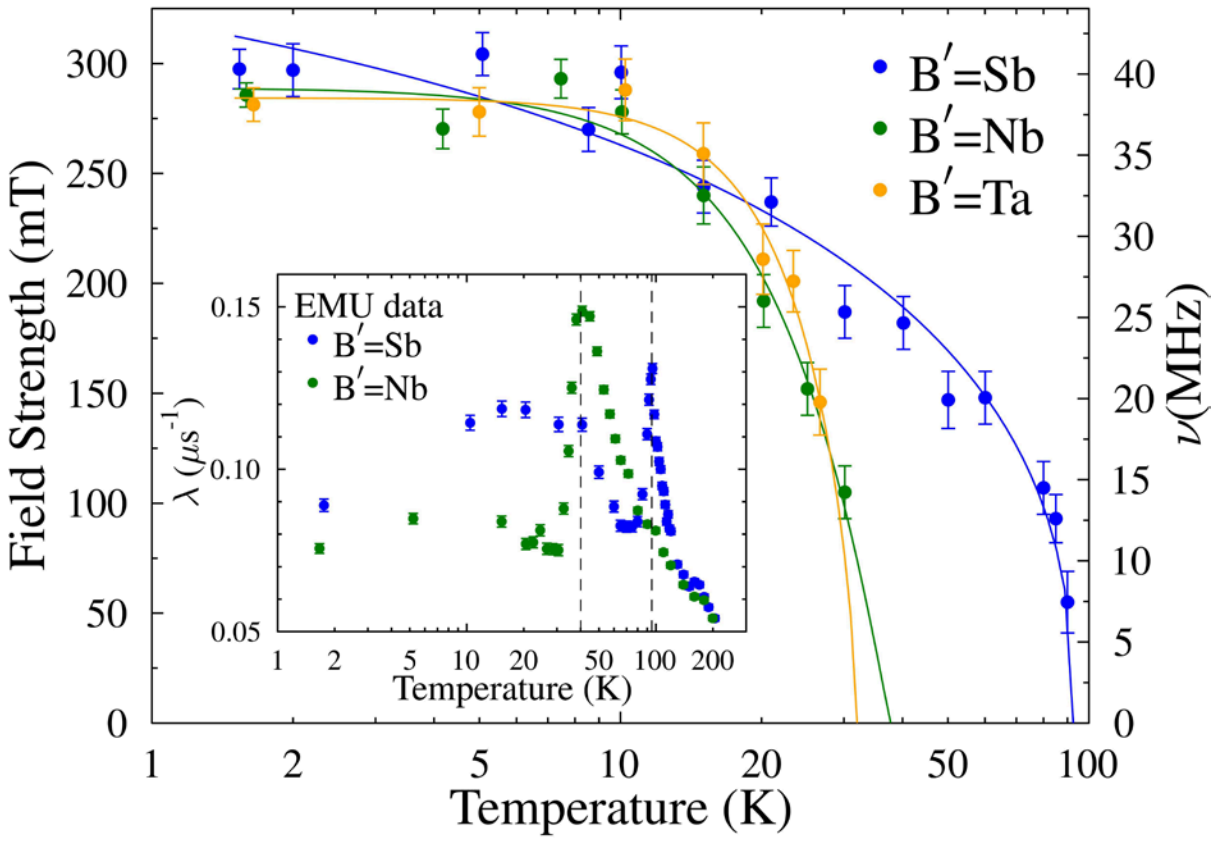
Field Strength (mT)
Temperature (K)
ν(MHz)
B′=Sb
B′=Nb
B′=Ta
EMU data
B′=Sb
B′=Nb
λ (μs⁻¹)
Temperature (K)

Figure 12